In-situ Formed Surface Complexes Promoting NIR-Light-Driven Carbonylation of Diamine with CO on Ultrathin $Co_2CO_3(OH)_2$ Nanosheets

Yingcong Wei [a], Wenying Zha [a], Lele Wang [a], Xiongfeng Ma [a], Shaohui Zhang [a], Rongjian Sa [b], Huaxiang Lin [a], Zhengxin Ding [a], Jinlin Long [a], Xianzhi Fu [a], Rusheng Yuan [a,*]

[a] State Key Laboratory of Photocatalysis on Energy and Environment, College of Chemistry, Fuzhou University, Fuzhou 350108, PR China
[b] Institute of Oceanography, Ocean College, Minjiang University, Fuzhou, Fujian 350108, PR China

ARTICLE INFO

ABSTRACT

Tailoring the surficial chemical environment of two-dimensional materials by organic modification is an effective way to optimize their catalytic behaviors. Herein, we present a dynamic coordination approach to improve the photocatalytic performance of ultrathin $Co_2CO_3(OH)_2$ nanosheets (u-CoCH) in NIR light ($\lambda > 780$ nm) driven carbonylation reaction by using the reacting substrates (diamines) as the ligands. The coordination of diamines with surface Co^{2+} ions form a binuclear complex at the crystallographic planes of u-CoCH. The as-formed complexes can reduce the energy barrier of carbonylation reaction by weaking the N-H bond of the substrate on u-CoCH, and afford enhanced light response as well as the prolonged photogenerated electron lifetime. Together with the successful synthesis of a series of important structural motifs in pharmaceuticals and bioactive agents, the promoted photosynthesis reaction mode via in-situ formed surface complexes offers a model toward full-spectrum-solar-energy conversion in the field of chemical synthesis.

1. Introduction

The organic modification on metal-based heterogeneous catalysts has emerged as an effective strategy to optimize their catalytic performance by inducing both electronic and 3D steric effects [1–4]. Unfortunately, most of the introduced organic modifiers may prevent the full exposure of active centers to target molecules on catalytic interface, which will offset the optimization partially [1,5,6]. For this issue, one exception is that the reacting substrates serve as the coordinating ligands thus modifying the heterogeneous catalysts [7]. Such a strategy ensures a continuous conversion of the ligands to non-coordinating products on the surface of catalysts and thus propagate the reaction sustainably. This subtly alternative reduces the contact resistances between the substrates and the modified catalysts, and affords a stable dispersion of nano-catalysts in polar media [7]. However, the change of the interfacial microstructure of the catalysts at molecular level is still unclear during ligand exchanging, which results in limited success in applying this strategy for a wider range of catalytic transformation especially in more complicated multi-phase reactions towards the synthesis of fine chemicals.

Metal-based heterogeneous catalysts are prone to distortion of the local structure when ligands adsorb on metal centers [8,9]. Due to the strong σ-donor properties of the nitrogen-donors, amine has been regarded as an important organic ligand to alter the electronic structures of the metal atoms [10]. Following nitrogen donor ligands (L1) adsorption, central metal atom with empty d orbitals can accept the lone pair electrons from N atom and then donates part of electrons back to ligands [11]. This charge transfer modifies electronic structure of the metal atom, as well as induces N-H bond weakening, promoting the dehydrogenation of amines [12]. Notably, part of electrons transferring from central metal atom to the uncovered surface atoms nearby make the surface highly electron rich, resulting in a considerable enhanced adsorption of electron-withdrawing ligands (L2), such as CO [13,14]. In the case of CO ligand, the electrons are donated from d orbitals of central metal atom back into the CO $2\pi^*$ orbitals, benefitting for the activation of CO [15]. As a synthetically attempt, these results encourage us to reason that a simultaneous activation of L1 as well as L2 ligands can be fulfilled on the same catalysts surface to generate ureas via the carbonylation reaction. Since the functional group in ureas always existing in pharmaceutical candidates, agrochemicals, resin precursors, dyes and additives to petrochemicals and polymers, the synthesis of ureas remains of interest [16–18]. Generally, complexes of several

transition metals including Ni, [19] Pd, [20] Ru, [21] Cu, [22] and Co [23] as well as main-group elements such as sulfur and selenium were used in the catalytic conversion of primary amines and CO to acyclic ureas [24]. However, catalytic carbonylation of diamines with CO to cyclic ureas are still limited. Present works mainly focus on the noble metals such as Pd, Rh, and Ir catalysts [25,26]. Even these catalysts could afford excellent catalytic activity in carbonylation reactions, P-, N-, and C-based ligands are inevitable in these reactions. Thus, the

development of new synthetic protocols for the catalytic synthesis of ureas has attracted attention. Given that Co atom possess vacant d atom orbit and high affinity toward π bonds, Co-based catalysts have shown great potential in coordinating with ligand molecules featuring unpaired electrons such as CO and amines.

Given that Co atom possess vacant d atom orbit and high affinity toward π bonds, Co-based catalysts have shown great potential in coordinating with ligand molecules featuring unpaired electrons such as
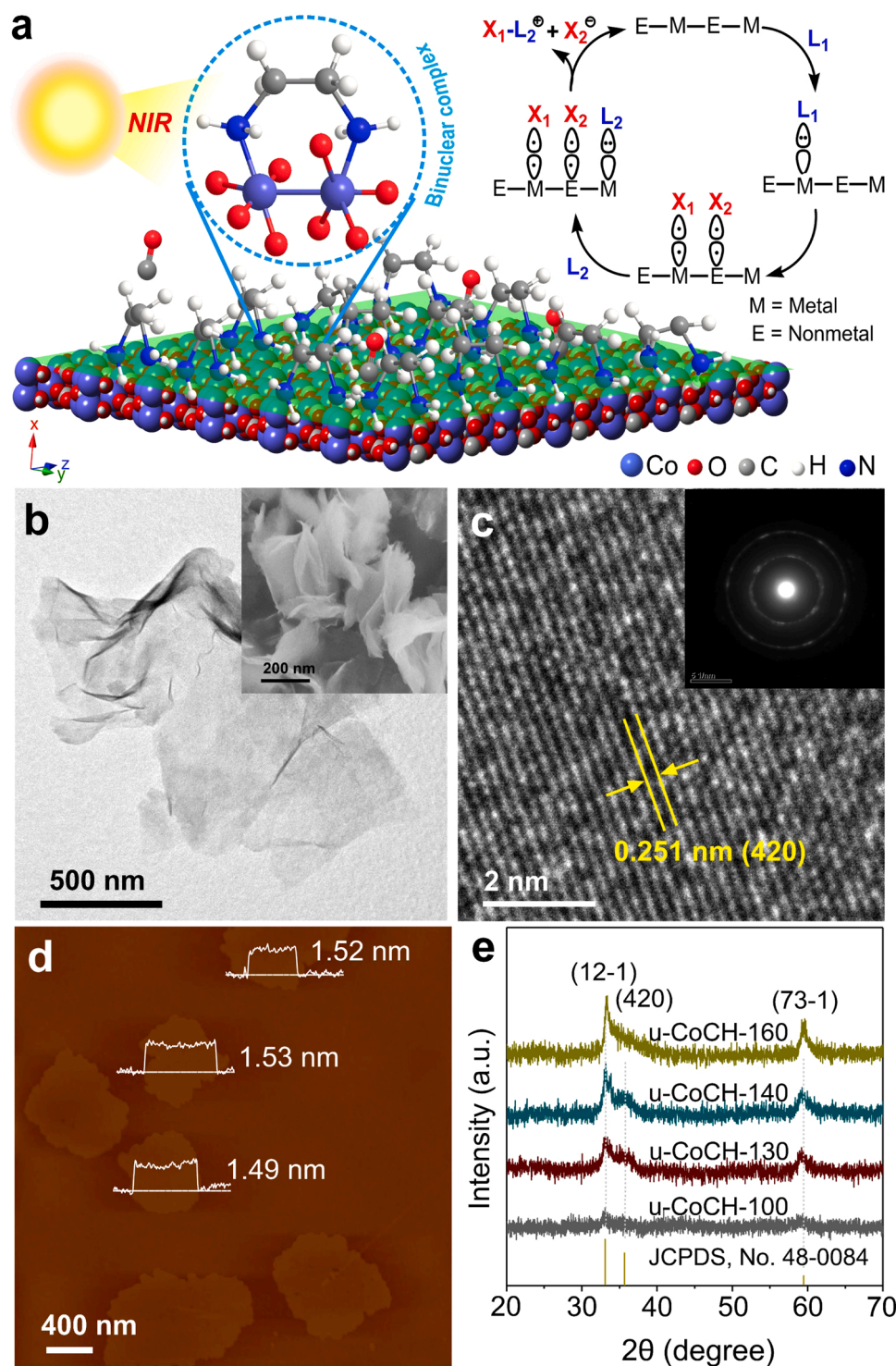

Fig. 1. (a) The in-situ formed binuclear complex at the interface of diamine and $Co_2CO_3(OH)_2$. (b) TEM and SEM (inset) images of u-CoCH-140. (c) HRTEM images and the corresponding electron diffraction patterns (inset) of u-CoCH-140. (d) AFM image and corresponding height profiles of u-CoCH-140. (e) XRD spectra of u-CoCH.

CO and amines [27–29]. Therefore, we here employed ultrathin $Co_2CO_3(OH)_2$ nanosheets (u-CoCH) to proceed photocatalytic carbonylation reaction of diamines with CO to synthesize cyclic ureas (19 samples) under low-energy NIR light (> 780 nm) excitation, in which surficial chemical environment of the catalysts can be adjusted effectively via diamine coordination (Fig. 1a). The coordination of diamine molecules with coordinatively unsaturated surface Co^{2+} ions formed binuclear complexes at crystallographic planes of u-CoCH, which provided abundant active sites as well as enhanced solar light absorption ability. The formed complexes also induced N-H bond weakening to favor the activation of diamine molecules into nitrogen-centered radicals, and further reacting with CO to yield cyclic ureas under NIR light radiation. The conversion of substrates (ligands) into non-coordinating products chemically drives the sustained ligand displacement on u-CoCH surface, ensuring the continuous regeneration of the active sites. In this work, CoCH nanosheets were found to be remarkably active for the oxidative carbonylation of diamine to cyclic urea using CO as the carbonyl source.

2. Experimental section

2.1. Materials and reagents

All chemicals were used without further purification. Cobalt salts, ethylene glycol and sodium carbonate were purchased from Alfa Aesar. N,N-Dimethylformamide (DMF), N,N-dimethylacetamide (DMAc), dimethyl sulfoxide (DMSO), acetonitrile and cyclohexane (CYH) were obtained from Sinopharm Chemical Technology Co. Ltd. Diamines were obtained from Aladdin.

2.2. Catalyst preparation

2.2.1. Synthesis of CoCH nanosheets with different crystallinities

In a typical procedure, 0.02 mmol cobalt(II) acetate tetrahydrate was added into a mixed solution of 5 mL octylamine and 60 mL ethylene glycol. Then, the mixture was gradually heated to the preset temperature followed by vigorous stirring under nitrogen atmosphere. Then, 200 mL Na_2CO_3 solution (0.02 M) was quickly added and remained at a temperature of 140 °C for 1 h. The reaction system was allowed to cool down to room temperature naturally, the obtained products were then collected by centrifuging the mixture, washed with cyclohexane and H_2O for several times, and then dried at 80 °C in vacuum overnight. Finally, solid catalysts (named as u-CoCH-140) were collected after heat treatment under N_2 at 120 °C in a tubular furnace for further characterization. Similar preparation methods were used for the synthesis of CoCH nanosheets with different crystallinities (named as u-CoCH-100, u-CoCH-130, and u-CoCH-160) except that the reactions were conducted at 100 °C for 0.3 h, 130 °C for 1 h and 160 °C for 3.5 h, respectively.

2.2.2. Synthesis of CoCH nanorods

The synthesis procedure was same as the u-CoCH-160 but no octylamine was added into the reaction system.

2.2.3. Synthesis of CoCH nanoparticles

CoCH nanoparticles were synthesized following the same procedure as the CoCH nanorods but precipitated at 80 °C.

2.2.4. Synthesis of Co_3O_4 nanosheets

In a typical procedure, the as-obtained u-CoCH-140 nanosheets were calcined at 350 °C for 1 h in air. Then, the obtained black powders were collected for further characterization.

2.2.5. Synthesis of CoO nanosheets

In a typical procedure, the as-obtained u-CoCH-140 nanosheets were calcined at 350 °C for 1.5 h in N_2. Then, the obtained black powders were collected for further characterization.

2.3. Characterization

The X-ray diffraction (XRD) patterns were collected by a Bruker D8 Advance X-ray diffractometer with Cu Ka radiation (λ = 1.54178 Å). The field emission scanning electron microscopy (FESEM) measurement was measured on a Hitachi SU8010 instrument. Transmission electron microscope (TEM) images, HRTEM images, elemental mapping and EDX-spectra were obtained using a Hitachi-7700 instrument. Atomic Force Microscopy (AFM) was measured on a Bruker Dimension Icon. The N_2 adsorption/desorption isotherms were obtained using a Micromeritics 3500 adsorption instrument at 77 K. The X-ray photoelectron spectra (XPS) were analyzed on an ESCALAB 250 photoelectron spectrometer with Al Kα as the excitation source, and C 1 s (284.6 eV) as a reference. Ultraviolet-visible diffuse reflectance spectroscopy (DRS) was performed on a Varian Cary 500 Scan spectrophotometer, using $BaSO_4$ as reference. Raman spectra were obtained using a Renishaw invia Raman microscope (Renishaw InVia Raman, UK). ^1H and ^{13}C NMR spectrums were recorded at 600 MHz using JEOL JNM-ECZR-600 NMR spectrometers. The inductively coupled plasma atomic emission spectrometry (ICP-AES) was carried out using a Thermo Scientific iCAP 7400. LC–QTOF-MS spectrum was recorded at G6520B. Thermogravimetric analysis (TGA) was measured on a STA449C/6/G thermal gravimetric analyzer under flowing air with a heat rate of 10 °C min-1 from 50° to 800 °C. The TG/IR analysis was performed by using a TG/IR system combining with a Netzsch 209 TG analyzer and a Brüker Vector 22 FT-IR spectrometer. The in-situ FTIR spectra of EDA adsorbed on the samples were recorded on a Nicolet Nexus 670 Fourier transform infrared (FT-IR) spectrometer in the range of wavenumber from 600 to 4000 cm^{-1}. The 600 nm light, 800 nm light , visible to near-infrared (NIR) light (λ = 350–1050 nm) and the NIR light (λ = 780–1050 nm) light used in this study is provided by a 300 W xenon lamp (PLS-SXE300D, Beijing Perfect Light co. Ltd, China) equipped with different cutoff filters. UV light (254 nm) is provided by 4-W UV lamps with certain wavelengths centered at 254 (Philips, TUV 4 W/G4 T5 or TL 4 W/05). The irradiance spectra of the incident lights were provided in Fig. S1.

2.4. Calculation of the photothermal conversion efficiency

The photothermal conversion efficiency (η) of u-CoCH-140 was calculated according to the following equations:

$$\eta = \frac{hA(\Delta T_{max,mix} - \Delta T_{max,H_2O})}{I(1 - 10^{-A_\lambda})} \tag{E1}$$

$$\theta = \frac{\Delta T}{\Delta T max} \tag{E2}$$

where h and A was the heat transfer coefficient and surface area of the container, respectively. $\Delta T_{max, mix}$ and $\Delta T_{max, H2O}$ were the change in temperature of the u-CoCH-140 dispersion and H_2O at the maximum temperature at steady state, respectively. I was the power of laser, and A_λ was the absorbance of u-CoCH at 808 nm. θ is a dimensionless driving force of temperature.

2.5. Computational details

All the calculations were performed based on spin-polarized periodic density functional theory (DFT) implemented in Vienna ab initio simulation package (VASP) [30–32]. The electron-ion interactions were described by the projector augmented wave (PAW) method and the electron exchange and correlation energy were treated with the gradient corrected Perdew-Burke-Ernzerh (GGA-PBE) functional [33,34]. The kinetic cutoff energy for plane-wave basis set was set to be 350 eV. For

the geometric optimization of bulk CoCH composed of 8 Cobalt atoms, 4 Carbon atoms, 20 Oxygen atoms and 8 Hydrogen atoms, the total energy convergence was set to be lower than 10^{-5} eV, and the force convergence was set to be smaller than 0.05 eV/Å. Electron smearing of $\sigma = 0$ eV was used following the Methfessel-Paxton scheme [35]. Brillouin zone sampling was employed using a Monkhorst-Packing grid $2 \times 2 \times 1$, and we also used a $3 \times 3 \times 1$ κ-points grid for density of state (DOS), band structure. The [111]-oriented u-CoCH nanosheets were simulated by periodically repeating the atomic layers along the [111] direction of the unit cell. Each CoCH layer model was separated by a vacuum region of 15 Å. The adsorption energies E_{ad} are defined as follows,

$$E_{ad} = E_{total} - [E_{slab} + E_{adsorbate}] \tag{E3}$$

where E_{total}, E_{slab} and $E_{adsorbate}$ represent the optimized total energies for the slabs with adsorbate molecules, the energy of the clean slab of the surface and the energies of free adsorbate molecules, respectively.

The free energy was calculated by $\Delta G = \Delta E - T\Delta S + \Delta ZPE$. In detail, ΔE, $T\Delta S$ and ΔZPE represent reaction energy of dehydrogenation, the gas-phase entropy contribution at 298 K and the zero-point energy correction.

2.6. General procedure for photo-driven carbonylation of diamine with CO

The carbonylation reaction of 1, 3-diaminopropane was used as an example. $Co_2CO_3(OH)_2$ (10 mg) and 1, 3-diaminopropane (2 mL, 24 mmol) were introduced into a reactor (Schlenk tube) and kept in suspension by magnetic stirring. The reactor was sealed with a balloon which was filled with CO. After evacuation and CO backfill for several times, 5 mL of O_2 was injected into the reactor (Fig. S2 and S3). Then the reaction was conducted under illumination for 24 h. After reaction, filtrate from the suspension was collected, and then injected to an Agilent GC 7890 gas chromatographer to analyze the liquid composition.
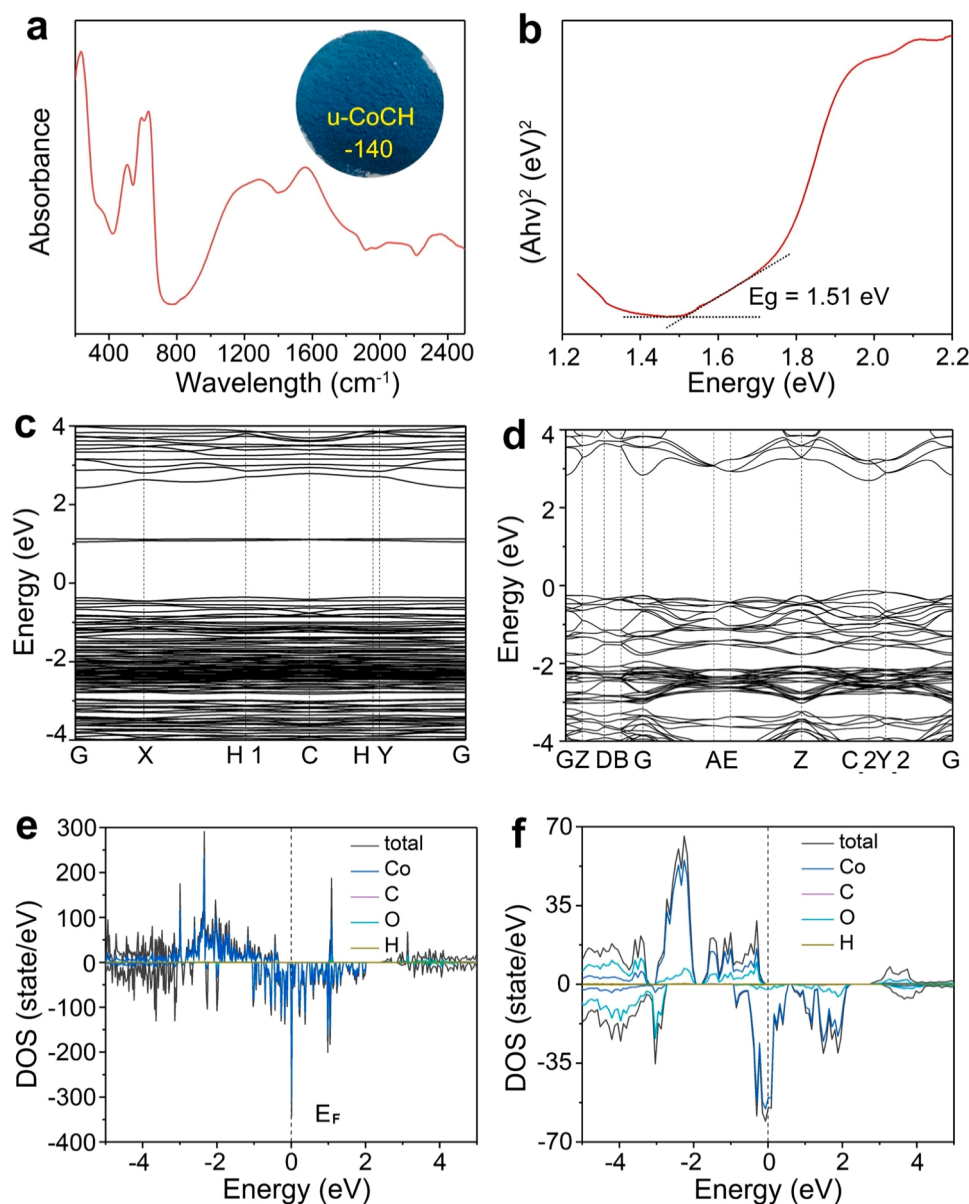

Fig. 2. (a) UV-Vis-NIR light absorption spectra and (b) corresponding optical bandgap of u-CoCH-140. The insert in (a) is the digital photographs. Calculated band structure for (c) CoCH nanosheet and (d) CoCH bulk. Normalized density of states (DOS) for (e) CoCH nanosheet and (f) CoCH bulk.

3. Results and discussion

3.1. Design and characterization of u-CoCH

A series of the $Co_2CO_3(OH)_2$ samples were firstly fabricated using a modified ligand-confined growth strategy (Fig. S4) [16,36]. The composition of the material was closely relevant to the structure of corresponding precursor. The structure and composition of the precursor were therefore characterized in detail. The corresponding precursor was $Co(CO_3)_{0.5}(OH)\cdot0.11H_2O$ confirmed by the corresponding XRD (Fig. S5) [26,37]. TGA curve showed that $Co(CO_3)_{0.5}(OH)\cdot0.11H_2O$ lost crystal water and became $Co_2CO_3(OH)_2$ after calcination at 120 °C under N_2 (Fig. S6). Typically, TEM, SEM and AFM images confirmed that

the partially crystalized samples are ultrathin nanosheets in shape, exhibiting an average thickness of about 1.5 nm (Fig. 1b-d and Figs. S7-S9). These two-dimensional (2D) nanosheets which nearly all the metal ions are exposed to be beneficial in spatial charge separation of the photocatalytic process. The EDS mapping and spectrum showed the elemental composition of Co (21.7 atom%), C (11.0 atom%) and O (67.3 atom%, Fig. S10). Further XRD analysis generally supported the judgment of monoclinic $Co_2CO_3(OH)_2$ of all differentially crystalized samples with the similar appearance of broaden diffraction peaks located at 33.2º, 35.5º and 59.3º (JCPDS, No. 48–0084, Fig. 1e) [38]. Another notable feature is that u-CoCH behaves a nearly full spectrum absorption covering.

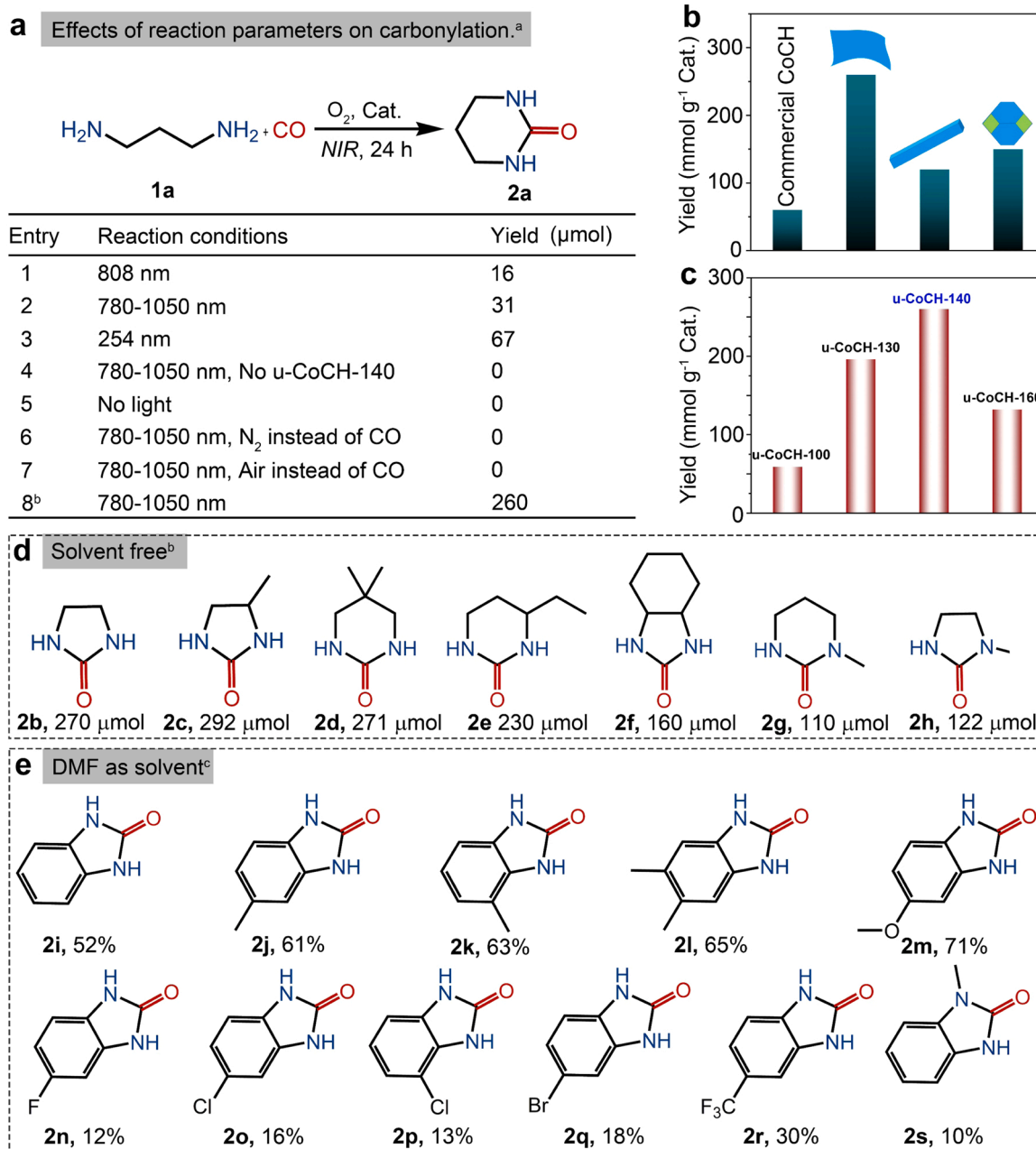250–2500 nm in UV-Vis-NIR region (Fig. 2a). The measured band

Fig. 3. (a) Carbonylation of diamine with CO and control experiments. Catalytic activities of CoCH catalysts with different (b) morphologies and (c) crystallinity under NIR light irradiation. (d,e) Substrate scope of diamines. [a]General conditions: 1 (2 mL), CO atmosphere (balloon pressure), u-CoCH-140 (10 mg), NIR light irradiation (808 nm, 10 mW·cm^{-2}, 780–1050 nm, 450 mW·cm^{-2}), UV light irradiation (254 nm, 10 mW·cm^{-2}), the reaction temperature was maintained at 25 °C by means of a circulation condensate device, GC yields. [b]NIR light irradiation (780–1050 nm, 450 mW·cm−2) for 24 h, and the circulating cooling water source was removed during the reactions. [c]1a (0.1 mmol), CO atmosphere (balloon pressure), u-CoCH-140 (4 mol%), DMF (0.1 M). Yield was determined by the GC.

gap (Eg) of u-CoCH-140 is 1.51 eV (Fig. 2b), closed to the calculated value of 1.42 eV in DFT mode (Fig. 2c) lower than that of u-CoCH bulk (Fig. 2d). Theoretically, a higher density of states (DOS) at the CB edges of CoCH nanosheet than that of its bulk counterpart will afford more easily electronic transition with certain light excitation (Fig. 2e,f) [39–41]. And the coordinately unsaturated Co atoms on u-CoCH can coordinate with the substrates through hybridization, leading to enhanced mass and electron transfer. All these results may signify that u-CoCH are good candidates to execute efficient photocatalysis with broad wavelengths of light excitation.

3.2. Photocatalytic carbonylation of diamine with CO

The redox activities of u-CoCH under NIR light excitation were tested using the carbonylation reaction of diamine with atmospheric pressure of CO to afford cyclic ureas which were vital heterocyclic motifs in biologically active molecules [42–44]. Interestingly, when the u-CoCH-140 is dissolved in 1,3-diaminopropane (**1a**), the carbonyl insertion of **1a** occurs to generate a small amount of tetrahydro-2-pyrimidinone (**2a**) upon 808 nm NIR light irradiation under solvent-free conditions (Fig. 3a, entry 1). Upon irradiation with an enhanced intensity of NIR light (780–1050 nm) or a shorter wavelength (254 nm), the increased **2a** yields of 31 and 67 µmol are observed, respectively (entries 2 and 3). The transformation hardly take place in the absence of u-CoCH or light (entries 4 and 5). This preliminarily verifies that the carbonylation process is in a typical photocatalytic mode with u-CoCH as the photocatalyst. No **2a** is obtained when N_2 or Air instead of CO is used, suggesting CO is the only carbonyl source rather than the CO_3^{2-} in u-CoCH sample or the CO_2 in the air (entries 6 and 7). Furthermore, the [13]CO labeling experiments was also conducted, and the results were displayed in the Fig. R1. When CO was replaced by [13]CO (^{13}C, 99%), the corresponding ^{13}C-label-ed-tetrahydro-2-pyrimidinone (**2a**) was detected in the GC-MS spectra after 24 h NIR light irradiation (Fig. S11). When the circulating cooling water source used to temperature control is removed, the yield of **2a** is considerably increased up to 260 µmol, accompanied by a significant temperature rise of the rection mixture (entry 8). After 24 h's light irradiation, 82 µmol **2a** was detected indicating the effective of 600 nm light irradiation. Even under sunlight irradiation, the carbonylation reaction proceeds smoothly and gives 55 µmol of **2a** (Fig. S12). Obviously, the u-CoCH may undergo a photothermal conversion process when.

dissolved in **1a**, and such a thermal effect can promote the reaction further. Extend the reaction time to 96 h, the reaction can also proceed and the production of **2a** can reach to 720 µmol (Fig. S13-S15). The TON value of $Co_2CO_3(OH)_2$ nanosheets was up to 15.3, indicating their catalytic characteristics during the reaction. However, under dark conditions the reaction cannot occur when the temperature is lower than 40 °C, but the yield of **2a** increases as the reaction temperature raises from 40 °C to 80 °C (Fig. S16). Even heated to 80 °C, the yield of **2a** is still lower than that upon NIR light excitation. Furthermore, the yield of **2a** increases with the increase of incident photons (Fig. S17). These results indicate that the photocatalytic process plays a dominant role in this reaction.

Effects of the morphology and crystallinity of the catalysts on catalytic activity were also elucidated. When commercial CoCH, rod-like CoCH and CoCH nanoparticles were employed as the catalysts, the reactions could take place and give lower yields of **2a** than CoCH nanosheets, which identified the superiority of atomic thickness structure (Fig. 3b, S18 and S19). The catalytic activity is also relevant with the crystallinity of the catalyst but no direct correlation with their surface areas (Fig. 3c and S20). However, a series of cobalt salts ($CoCl_2$, $CoCl_2 \cdot 6 H_2O$, $Co(Ac)_2 \cdot 4 H_2O$ and $Co(NO_3)_2$) all afforded very low yield of **2a** (≤ 15 µmol, Table S1 entries 1–4). $CoCO_3$ and cobalt oxide such as Co_2O_3, Co_3O_4 and CoO can hardly drive the reaction, while $Co(OH)_2$ afforded a lower yield of **2a** (125 µmol) than u-CoCH (Table S1 entries 5–9). When the Co(II) on u-CoCH was partially oxidized to be Co(III), a

lower yield of **2a** was obtained (Figs. S21-S23). All these results show that the high catalytic activity is more related to the Co(II) on CoCH nanosheets rather than the Co(III) or free Co(II) ions in solution (Fig. S24, Table S2). Moreover, the di-anion (OH⁻, CO_3^{2-}) in u-CoCH may endow the interface with dragging H from N functionality, thus promoting the carbonylation reaction [45–47]. As shown in Fig. S25, the used u-CoCH-140 remains the two-dimensional flake. The u-CoCH catalysts were tested for 3 more cycles, and no degradation in performance (Fig. S26). When the reaction system was scaled up to 10- and 30-mL, nearly 4- and 11-fold enhancement on the yield can be obtained, respectively (Table S1, entries 10 and 11), illustrating their industrial production potential of this u-CoCH catalytic system.

Kinetic experiments with different concentration of CO (100%, 85%, 70%, 55%, 40% and 25%) and **1a** (100%, 75%, 50% and 25%) are performed to provide insight into the role of CO and **1a**. The reaction rate decreases with the decrease of CO and **1a** concentration (Fig. S27a, c). Reaction order n_{CO} and n_{1a} can be calculated according to eq. 1 to be 0.7 and 2.1, respectively (Fig. S27b,d).

3.3. Substrate scope of carbonylation of diamine with CO

Furthermore, the proposed strategy exhibited good tolerance to a diverse range of diamines, for all the diamines appeared in Fig. 3d could react with CO to generate corresponding cyclic ureas in moderate to good yields. Ethylenediamines (EDA) could also afford five- membered cyclic urea (**2b**) with a yield of 270 µmol. When introducing electron-donating substituents into α-C atoms of EDA or 1,3-diaminopropane, desired products of **2c** and **2d** with higher production of 292 and 271 µmol were obtained, respectively. However, the introduction of ethyl group at primary C atom of 1,3-diaminopropane could result in lower yield of **2e** with 230 µmol due to the steric effect. To our delight, the 1,2-diaminocyclohexane can also react with CO to give hexahydro-2-benzimidazolinon (**2f**) with a moderate yield of 160 µmol. The introduction of methyl group on the N atoms of EDA or 1,3-diaminopropane would give lower desired ureas than that in the α-C atoms (**2g, 2h**). Furthermore, various solid diamines were also examined to explore potential applications of this catalytic system by adding suitable solvents (Table S3). We began our study by choosing o-phenylenediamine as the model substrate. After extensive optimization, the combination of u-CoCH-140 (4 mol%) in DMF (0.1 M) can afford corresponding product in 52% yield (entry 1). The carbonylation reaction of o-phenylenediamine with different functional groups proceeds smoothly and furnishes the corresponding ureas products with moderate to good yields of 13–71% (Fig. 3e). Obviously, o-phenylenediamine bearing electron-donating groups (**2j-2m**) give higher yields of products than that of electron-withdrawing groups (**2n-2r**). In addition, o-phenylenediamine with the functional groups on the N is demonstrated to be effective in this transformation (**2s**). Based on the above results, one can safely conclude that u-CoCH-140 exhibit preeminent photocatalytic performance with good tolerance to a diverse range of diamines.

3.4. Photothermal behavior and thermodynamic stability of u-CoCH

When the 1,3-diaminopropane (2 mL)-u-CoCH (10 mg) system was irradiated by NIR light (780–1050 nm) for 12 min, a net elevation in temperature of about 40 °C could be obtained with the involvement of u-CoCH-140 powders (Fig. 4a). Remarkably, when the system was irradiated with NIR (450 mW/cm²) light for 16 min, the measured temperature roses from 18 to.

80 °C, near to the optimum temperature. And, the measured temperature of the solution is closely related to the light wavelength (Fig. 4b,c). The photothermal conversion efficiency (η) of u-CoCH is calculated to be about 21.8%, indicating the preeminent solar light conversion efficiency (other relevant results and calculation details can be found in Fig. 4d-f). Thus, a photo-initiated thermal effect further contributes to the ptohocatalytic transformation of diamine during
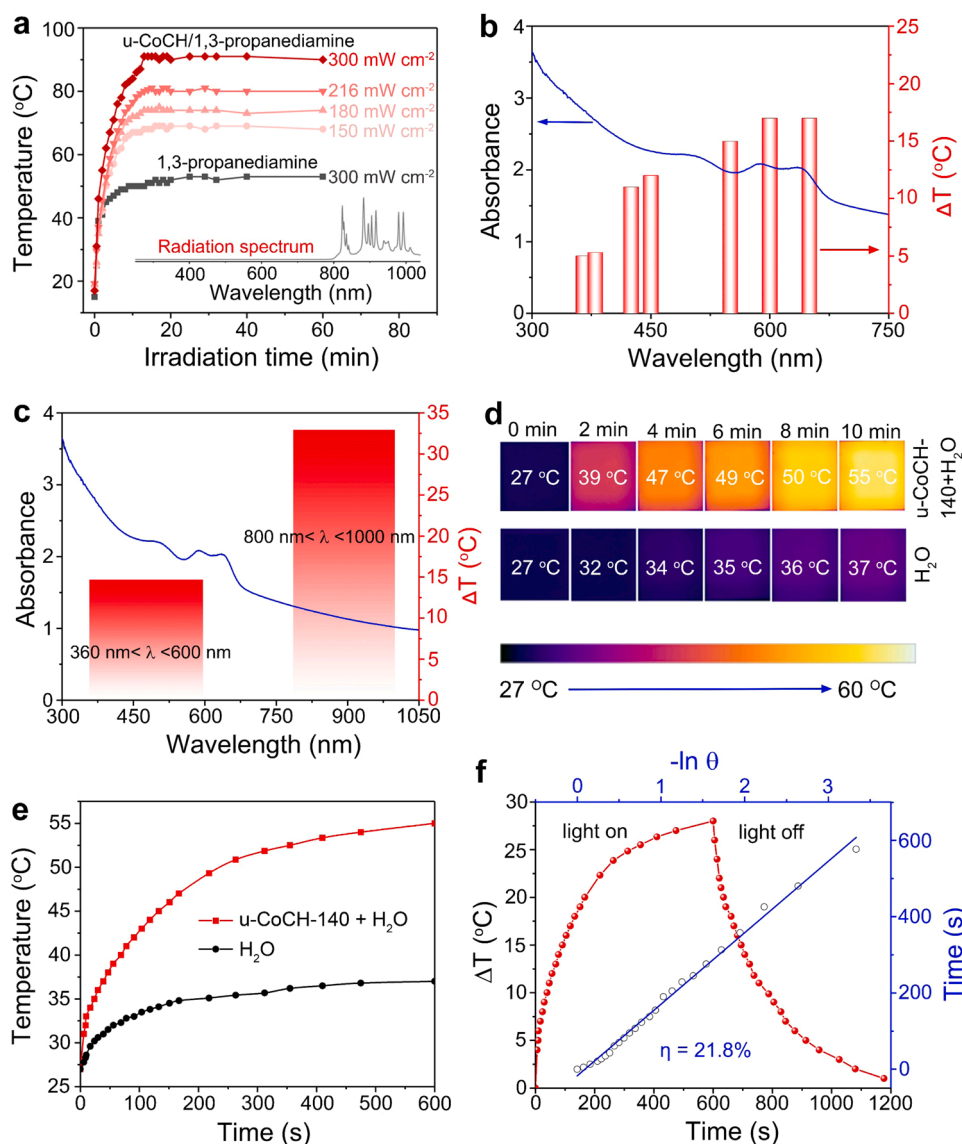
Fig. 4. (a) Heating curves of u-CoCH-140 (10 mg) in 1,3-diaminopropane (2 mL) under NIR irradiation with different light intensities. (b,c) Temperature elevation with irradiation at different wavelength. (d) Infrared thermal images. (e) Heating curves of u-CoCH-140 in u-CoCH-140/H_2O (100 μg mL^{-1}), and H_2O as reference under 808 nm irradiation. (f) Temperature change (ΔT) under light on-off irradiation and calculation of photothermal conversion efficiency.

reaction. Moreover, the ab initio molecular dynamics (AIMD) simulations, TG-IR images and thermogravimetric curve confirm the high thermodynamic stability of u-CoCH, ensuring the catalysts are suitable to operation under optimized temperature. (Figs. S28-S30).

3.5. Structure–activity relationship of u-CoCH

The Raman spectra of EDA-u-CoCH-140 show a peak centered at 371 cm^{-1}, which is assigned to T_{2g} Co-N band (Fig. 5a,b) [48]. And a new peak at 928 cm^{-1} appears in the FTIR spectra of EDA-u-CoCH-140 attributing to Co-N bond (Fig. 5c) [49]. All the results above indicate the formation of coordination bonds between Co and N. In order to elucidate the chemical adsorption characteristics of CO, in situ DRIFT spectra of EDA-u-CoCH catalysts under 1% CO flow was measured. As shown in Fig. 5d, the peaks at 2117 and 2173 cm^{-1} are assigned to the stretching vibration of the gas phase CO molecules [50]. A new peak appeared at 2106 cm^{-1} as adsorption time is extended, which is assigned to the linear adsorption of CO on the surface of EDA-u-CoCH [51].

To give an in-depth understanding for the origin of the outstanding catalytic performance of u-CoCH, the effect of diamines chemisorption on the surface electronic structure was investigated by XPS analysis. From the high-resolution XPS spectra, the peaks of Co 2p in u-CoCH-140 with EDA chemisorbed on their surfaces (denoted as EDA-u-CoCH-140) shifts to higher binding energies than that of pristine u-CoCH-140, suggesting the decrease of the electron density for Co element caused by the coordination (Fig. 6a) [52–55]. The FT-IR spectra show that the ωN-H signal of EDA shifts from 1552 to 1506 cm^{-1} after being adsorbed on the u-CoCH-140 (Fig. 6b), indicating the N-H bond weakening induced by coordination [56,57]. Furthermore, the adsorption of EDA on u-CoCH-140 can largely enhance the absorption intensity in a wide range of 250–2500 nm (Fig. 6c and S31), which may be attributed to the formation of Co-N bond and increased disorder in the surface layers of catalysts thus promotes electron migration between u-CoCH and EDA. Moreover, EDA-u-CoCH-140 exhibits a longer average fluorescence lifetime (τ = 7.52 ns).

than that of pristine u-CoCH-140 (τ = 6.37 ns, Fig. 6d). The possible configurations and the corresponding adsorption energy of EDA adsorbed on CoCH (111) surface are calculated. The optimized structures including 1) bidentate (two N bonding to two adjacent cobalt, Figs. 7a), 2) monodentate I (one N bonding to one hexa-coordinated cobalt,
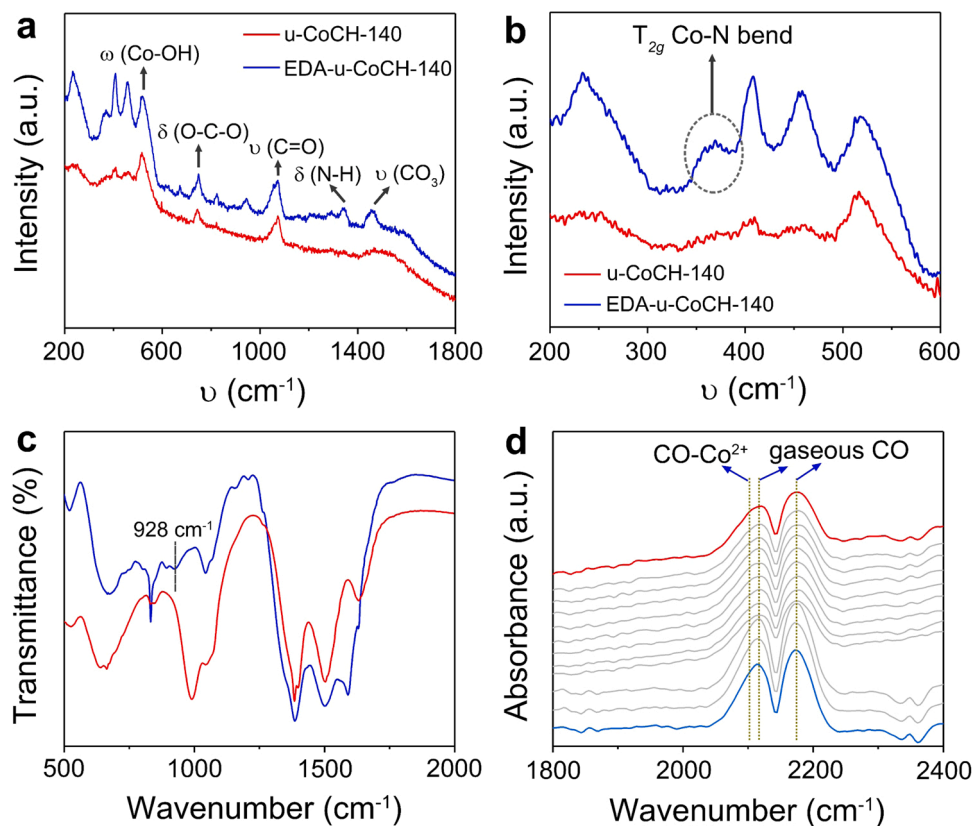
Fig. 5. (a,b) Raman spectra and (c) FTIR for structures of the surface complexes.(d) *In situ* DRIFTS of CO adsorbed over EDA-u-CoCH-140.
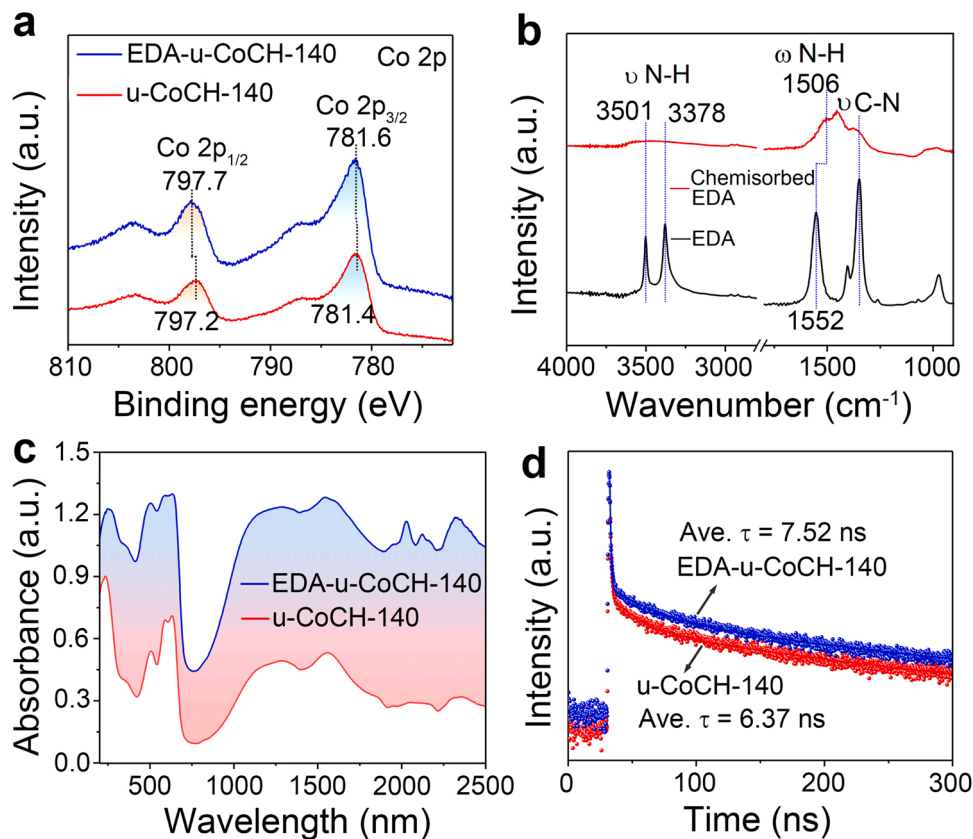

Fig. 6. (a) High-resolution XPS spectra of Co 2p, (b) In situ FTIR spectra for free EDA and EDA adsorbed on u-CoCH-140. (c) DRS spectra and(d) TRPL spectra of u-CoCH and EDA-u-CoCH-140.
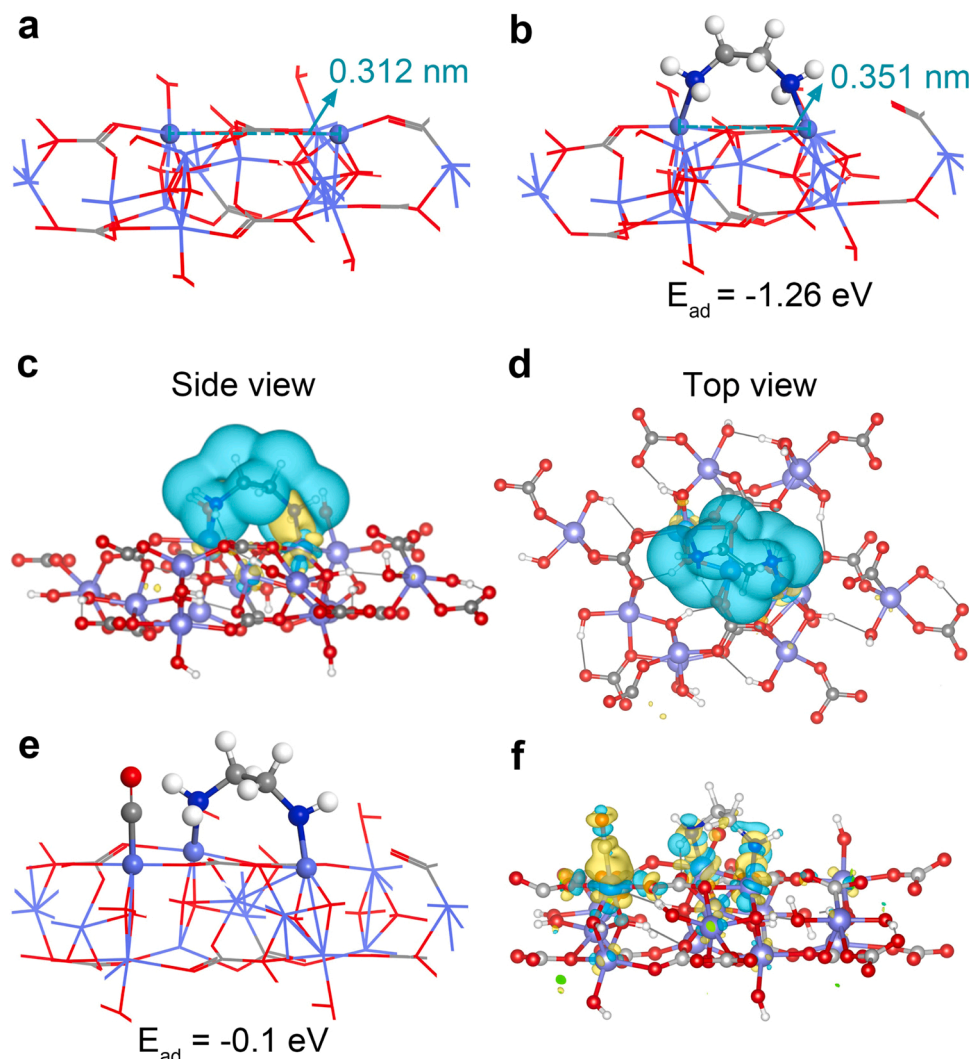
Fig. 7. The optimized geometric structure of (a) CoCH and (b) EDA adsorbed on CoCH (111). (c) Side view and (d) top view charge density difference of EDA adsorbed on CoCH (111). (e) The optimized geometric structures and (f) charge density difference of EDA and CO co-adsorbed on CoCH (111). The isosurface value is 0.004 e/Bohr³.

Fig. S32a), and 3) monodentate II (one N bonding to one penta-coordinated cobalt, Fig. S32b) are all thermodynamically stable. Among these structural models, the bidentate one exhibits the lowest adsorption energy (E_{ad}) of -1.26 eV, which suggests that the coordination between Co(II) ions on u-CoCH and diamine molecules produce a bidentate complex during the reaction. Interestingly, the increased distance between two adjacent Co atoms from 0.312 nm to 0.351 nm suggests that coordination would also.

result in higher degree of surface disorder to u-CoCH (Fig. 7a,b). These results indicate that the formed bidentate complex accounts for the enhanced optical absorption and prolonged lifetime of photo-generated carriers which can boost the interfacial catalytic reactions.

Furthermore, the charge density difference and Bader charge of the

bidentate configuration were also calculated to investigate the interactions between N and Co atoms. As shown in Fig. 7c,d and Table 1, central Co atom possessing empty d orbitals is peculiarly prone to accept the lone-pair electrons of N and donate about 1.2 electrons back into the p orbital of N which is consistent with that in Co 2p XPS spectrum. In addition, the calculated bond dissociation free energy (BDFE).

of the N—H bond in EDA-u-CoCH is -0.47 eV or -0.41 eV, well below that of the free EDA molecule (1.93 eV), revealing the N-H bond cleavage as well as the formation of $C_2H_7N_2$ * and H* is thermodynamically favorable (Fig. 8a-d). Based on the calculation results, the formed H atom can be stably adsorbed on the O of CO_3^{2-} adjacent to hexa- or penta-coordinated Co, with the E_{ad} of 0.33 or 0.36 eV, respectively (Fig. 8e,f). The above results reveal that the coordination of EDA to Co induces obviously weakening of N—H bond in diamine, benefitting for N–H activation which is the crucial step in the synthetic reactions relating to amines. Since the high stability of C≡O bond, the activation of CO has been the rate-determining step in the carbonylation reactions [58–60]. Therefore, the structural models of CO adsorbed (Fig. S33) and CO/EDA co-adsorbed (Fig. 7e) on CoCH (111) surface are also optimized. In the optimized co-adsorption model, CO is bonded to hexa-coordinated Co through the C atom with increased C≡O bond distance, and the co-adsorption energy is -0.1 eV. In addition, the calculated charge density difference (Fig. 7f) shows that electrons

Table 1
Bader charge analysis of $C_2H_8N_2$ on the penta-coordinate and hexa-coordinate cobalt atom of $Co_2CO_3(OH)_2(111)$ surface. Only the central and donor atoms are selected.

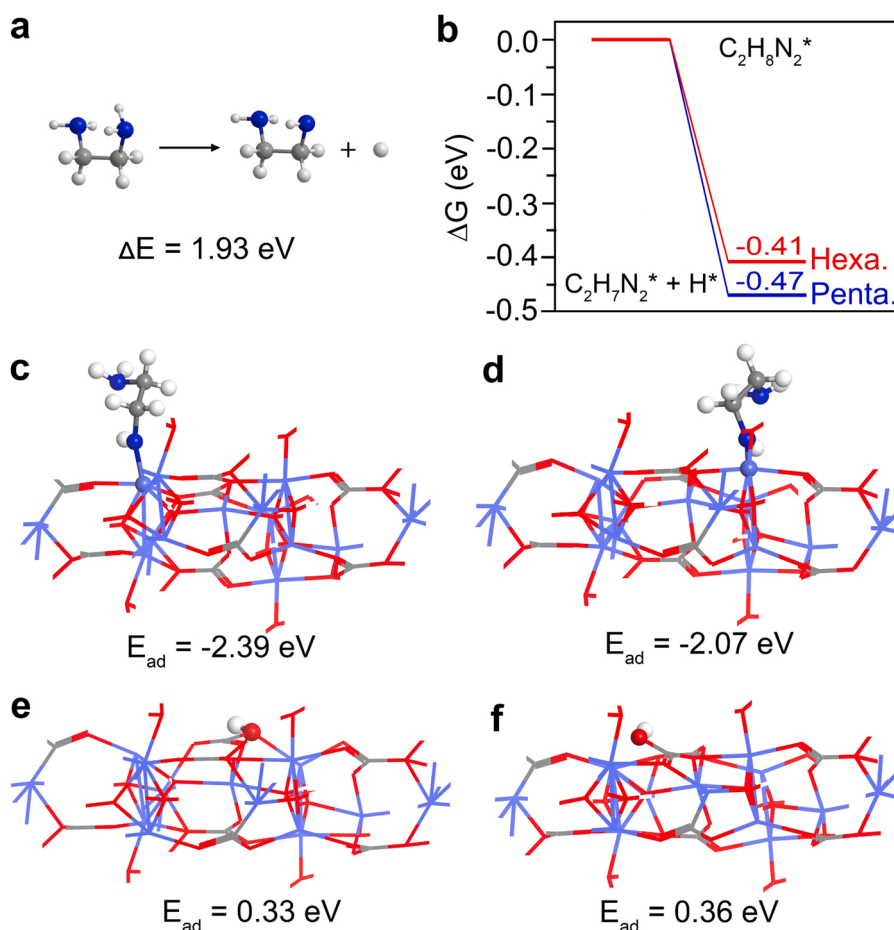| Penta-coordinate Atom	Charge transfer (e⁻)	Hexa-coordinate Atom	Charge transfer (e⁻)
Co	1.19	Co	1.11
N	-1.15	N	-1.17

Fig. 8. The reaction energies of dehydrogenation of (a) free ethylenediamine and (b) ethylenediamine molecule adsorbed on catalyst surface. (c) Configuration diagram of $C_2H_7N_2$ adsorbed on the surface penta-coordinated and (d) hexa-coordinated Co atom of $Co_2CO_3(OH)_2$ (111). Configuration diagram of H adsorbed on the surface O atom close to (e) penta-coordinated and (f) hexa-coordinated Co atom of $Co_2CO_3(OH)_2$ (111).

transfer from Co atom to C atom, illustrating CO acts as an electron acceptor in the adsorption configurations. This is consistent with the report that the strong C≡O bond is activated by π* back-donation from metal d orbitals to the π antibonding orbitals of the CO [61,62].

3.6. Reaction mechanism

To gather further insight into the key intermediate species of the cyclization carbonylation, trapping experiments were conducted. As shown in Fig. 9a and Table S4, the reaction is completely inhibited when TEMPO as a radical scavenger is added into the reaction mixture, which indicates that the radical intermediates are involved in this catalytic transformation. As evidenced in the LC-QTOF-MS spectrum, the·NH $(CH_2)_3NH$·as a key radical intermediate is identified through the signal for $[DMPO-NH·(CH_2)_3NH·-DMPO + H]^+$ (m/z = 299.2416) (Fig. 9b). Furthermore, H_2O is detected and the content increased with the prolonged reaction time according to ^1H NMR (Fig. 9c). The results prove that H_2O is the conceivable final form of H atom released from organic diamine.

Based on the above DFT calculation and experimental evidences above, the plausible reaction mechanism for photocatalytic carbonylation reaction of diamines over u-CoCH was proposed in Fig. 9d. As the fundamental step, the coordination of diamines with Co atom on the surface of.

u-CoCH (I) occurs and the complex (II) forms once adding the u-CoCH into diamines solution. Then the intramolecular deprotonation of II takes place to form intermediate III. This step is followed by intramolecular electron transfers from N to Co(II) in IV to give Co(I) (V) and

diamine radicals (VI) under NIR light irradiation. When these diamine radicals are exposed to CO atmosphere, the radical addition proceeds immediately to give corresponding cyclic urea products (VII). The reduced species Co(I) is then deoxidized into Co(II) species (I) by O_2, further initiating next catalytic cycles.

4. Conclusion

In conclusion, we propose a ligand-coordinating strategy employing substrates as organic ligands to tune the surface geometry and electronic structure of u-CoCH in photocatalytic carbonylation of diamine with CO. At the liquid–solid interface, a binuclear complex motif forms through the coordination between diamine molecules and adjacent Co^{2+} ions, which effectively reduces the energy barrier and thus leads to outstanding photocatalytic performance in the NIR light driven carbonylation. The in-depth study on the formed surface structure and its catalytic behaviors opens new avenues for optimizing the catalytic performance of heterogeneous catalysts, and provides critical insights for understanding the surface catalysis under two-dimensional materials.

CRediT authorship contribution statement

R.Y. conceived and initiated the research. Y.W. and L.W. designed and performed the experiments and wrote the manuscript. W.Z. and R.S. performed the DFT calculations. Y.W., L.W., X.M., S.Z. J.L. and H.L. analyzed the data and discussed the manuscript. Z.D. and X.F. supervised the research. All the authors commented on and approved the final
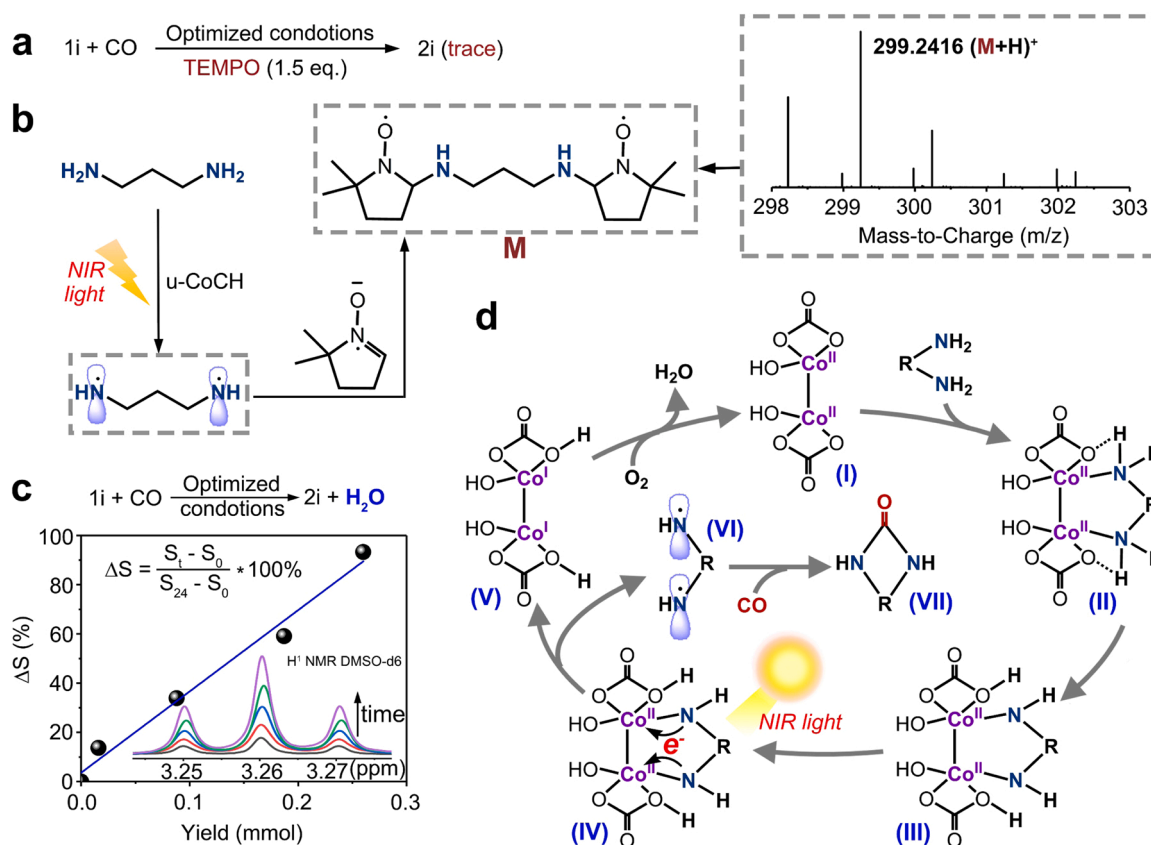
Fig. 9. (a) Radical-trapping experiment. (b) Capture and identification of N-centred radical by LCMS. (c) Detection of H_2O from the carbonylation reaction. (d) The proposed reaction mechanism.

manuscript.

Declaration of Competing Interest

The authors declare that they have no known competing financial interests or personal relationships that could have appeared to influence the work reported in this paper.

The authors declare no competing financial interest.

Appendix A. Supporting information

Supplementary data associated with this article can be found in the online version at doi:10.1016/j.apcatb.2022.121103.

References

[1] M.R. Narouz, K.M. Osten, P.J. Unsworth, R.W.Y. Man, K. Salorinne, S. Takano, R. Tomihara, S. Kaappa, S. Malola, C.T. Dinh, J.D. Padmos, K. Ayoo, P.J. Garrett, M. Nambo, J.H. Horton, E.H. Sargent, H. Häkkinen, T. Tsukuda, C.M. Crudden, N-heterocyclic carbene-functionalized magic-number gold nanoclusters, Nat. Chem. 11 (2019) 419–425.
[2] M. Ou, W. Tu, S. Yin, W. Xing, S. Wu, H. Wang, S. Wan, Q. Zhong, R. Xu, Amino-assisted anchoring of CsPbBr$_3$ perovskite quantum dots on porous g-C$_3$N$_4$ for enhanced photocatalytic CO$_2$ reduction, Angew. Chem. 130 (2018) 13758–13762.

[3] Z. Liu, B. Yan, S. Meng, R. Liu, W. Lu, J. Sheng, Y. Yi, A.-H. Lu, Plasma tuning local environment of hexagonal boron nitride for oxidative dehydrogenation of propane, Angew. Chem. Int. Ed. 60 (2021) 19691–19695.
[4] Renee W.Y. Man, C.H. Li, M.W.A. MacLean, O.V. Zenkina, M.T. Zamora, L. N. Saunders, A. Rousina-Webb, M. Nambo, C.M. Crudden, Ultrastable gold nanoparticles modified by bidentate N-heterocyclic carbene ligands, J. Am. Chem. Soc. 140 (2018) 1576–1579.
[5] W.L.B. Huey, J.E. Goldberger, Covalent functionalization of two-dimensional group 14 graphane analogues, Chem. Soc. Rev. 47 (2018) 6201–6223.
[6] E. Bekyarova, M.E. Itkis, P. Ramesh, C. Berger, M. Sprinkle, W.A. de Heer, R. C. Haddon, Chemical modification of epitaxial graphene: spontaneous grafting of aryl groups, J. Am. Chem. Soc. 131 (2009) 1336–1337.
[7] J. De Roo, I. Van Driessche, J.C. Martins, Z. Hens, Colloidal metal oxide nanocrystal catalysis by sustained chemically driven ligand displacement, Nat. Mater. 15 (2016) 517–521.
[8] J. Hulva, M. Meier, R. Bliem, Z. Jakub, F. Kraushofer, M. Schmid, U. Diebold, C. Franchini, G.S. Parkinson, Unraveling CO adsorption on model single-atom catalysts, Science 371 (2021) 375–379.
[9] J. López-Cabrelles, S. Mañas-Valero, I.J. Vitórica-Yrezábal, P.J. Bereciartua, J. A. Rodríguez-Velamazán, J.C. Waerenborgh, B.J.C. Vieira, D. Davidovikj, P. G. Steeneken, H.S.J. van der Zant, G. Mínguez Espallargas, E. Coronado, Isoreticular two-dimensional magnetic coordination polymers prepared through pre-synthetic ligand functionalization, Nat. Chem. 10 (2018) 1001–1007.
[10] Y.J. Kim, H.J. Kwon, I. Heo, I.S. Nam, B.K. Cho, J.W. Choung, M.S. Cha, G.K. Yeo, Mn–Fe/ZSM5 as a low-temperature SCR catalyst to remove NOx from diesel engine exhaust, Appl. Catal. B: Environ. 126 (2012) 9–21.
[11] S. Liu, Z. Cheng, Y. Liu, X. Gao, Y. Tan, Y. Ren, Z. Shen, Boosting electrochemical nitrogen reduction reaction performance of two-dimensional Mo porphyrin monolayers via turning the coordination environment, Phys. Chem. Chem. Phys. 23 (2021) 4178–4186.
[12] I. Pappas, P.J. Chirik, Ammonia synthesis by hydrogenolysis of titanium-nitrogen bonds using proton coupled electron transfer, J. Am. Chem. Soc. 137 (2015) 3498–3501.
[13] G. Chen, C. Xu, X. Huang, J. Ye, L. Gu, G. Li, Z. Tang, B. Wu, H. Yang, Z. Zhao, Z. Zhou, G. Fu, N. Zheng, Interfacial electronic effects control the reaction selectivity of platinum catalysts, Nat. Mater. 15 (2016) 564–569.
[14] I. Heo, J.W. Choung, P.S. I.S.Nam, Y.I. Song, C.B. In, G.K. Yeo, The alteration of the performance of field-aged Pd-based TWCs towards CO and C$_3$H$_6$ oxidation, Appl. Catal. B Environ. 92 (2009) 114–125.

[15] A. Berkefeld, W.E. Piers, M. Parvez, L. Castro, L. Maron, O. Eisenstein, Carbon monoxide activation via O-bound CO using decamethylscandocinium-hydridoborate ion pairs, J. Am. Chem. Soc. 134 (2012) 10843–10851.

[16] N. Volz, J. Clayden, The urea renaissance, Angew. Chem. Int. Ed. 50 (2011) 12148–12155.

[17] A.R. Katritzky, A. Oliferenko, A. Lomaka, M. Karelson, Six-membered cyclic ureas as HIV-1 protease inhibitors: a QSAR study based on CODESSA PRO approach, Bioorg. Med. Chem. Let. 12 (2002) 3453–3457.

[18] T. Nagai, N. Mimata, Y. Terada, C. Sebe, H. Shigehisa, Catalytic dealkylative synthesis of cyclic carbamates and ureas via hydrogen atom transfer and radical-polar crossover, Org. Lett. 22 (2020) 5522–5527.

[19] L. Cassar, M. Foa, Nickel-catalyzed carbonylation of aromatic halides at atmospheric pressure of carbon monoxide, J. Organomet. Chem. 51 (1973) 381–393.

[20] T. Kondo, Y. Tsuji, Y. Watanabe, Photochemical carbonylation of alkyl iodides in the presence of various metal carbonyls, Tetrahedron Lett. 29 (1988) 3833–3836.

[21] X.-F. Wu, H. Neumann, Ruthenium and rhodium-catalyzed carbonylation reactions, ChemCatChem 4 (2012) 447–458.

[22] F. Zhu, Y. Li, Z. Wang, X.F. Wu, Iridium-catalyzed carbonylative synthesis of chromenones from simple phenols and internal alkynes at atmospheric pressure, Angew. Chem. 128 (2016) 14357–14360.

[23] R.F. Heck, D.S. Breslow, The Reaction of cobalt hydrotetracarbonyl with olefins, J. Am. Chem. Soc. 83 (1961) 4023–4027.

[24] J. Ying, H. Wang, X. Qi, J.-B. Peng, X.-F. Wu, Base-promoted sulfur-mediated carbonylative cyclization of propargylic amines, Eur. J. Org. Chem. 2018 (2018) 688–692.

[25] F.P. Pruchnik, Organometallic Chemistry of Transition Elements, Springer Science & Business Media, 2013.

[26] Y. Wang, W. Ren, Y. Shi, An atom-economic approach to carboxylic acids via Pd-catalyzed direct addition of formic acid to olefins with acetic anhydride as a co-catalyst, Org. Biomol. Chem. 13 (2015) 8416–8419.

[27] X. Peng, K. Cheng, J. Kang, B. Gu, X. Yu, Q. Zhang, Y. Wang, Impact of hydrogenolysis on the selectivity of the Fischer-Tropsch synthesis: diesel fuel production over mesoporous zeolite-Y-supported cobalt nanoparticles, Angew. Chem. Int. Ed. 54 (2015) 4553–4556.

[28] J. Guo, H.D. Pham, Y.B. Wu, D. Zhang, X. Wang, Mechanism of cobalt-catalyzed direct aminocarbonylation of unactivated alkyl electrophiles: outer-sphere amine substitution to form amide bond, ACS Catal. 10 (2019) 1520–1527.

[29] M. Lautens, C.M. Crudden, Scope of the cobalt-catalyzed [2+ 2+ 2] homo-Diels-Alder reaction, Organometallics 8 (1989) 2733–2735.

[30] G. Kresse, J. Hafner, Ab initio molecular dynamics for liquid metals, Phys. Rev. B 47 (1993) 558–561.

[31] G. Kresse, J. Hafner, Ab initio molecular-dynamics simulation of the liquid-metal-amorphous-semiconductor transition in germanium, J. Phys. Rev. B 49 (1994) 14251–14269.

[32] G. Kresse, J. Furthmüller, Efficiency of ab-initio total energy calculations for metals and semiconductors using a plane-wave basis set, Comput. Mater. Sci. 6 (1996) 15–50.

[33] P.E. Blöchl, Projector augmented-wave method, Phys. Rev. B 50 (1994) 17953–17979.

[34] B. Hammer, L.B. Hansen, J.K. Nørskov, Improved adsorption energetics within density-functional theory using revised Perdew-Burke-Ernzerhof functionals, Phys. Rev. B 59 (1999) 7413–7421.

[35] T. Reier, Z. Pawolek, S. Cherevko, M. Bruns, T. Jones, D. Teschner, S. Selve, A. Bergmann, H.N. Nong, R. Schlögl, K.J.J. Mayrhofer, P. Strasser, Molecular insight in structure and activity of highly efficient, low-Ir Ir-Ni oxide catalysts for electrochemical water splitting (OER), J. Am. Chem. Soc. 137 (2015) 13031–13040.

[36] S. Gao, Z. Sun, W. Liu, X. Jiao, X. Zu, Q. Hu, Y. Sun, T. Yao, W. Zhang, S. Wei, Y. Xie, Atomic layer confined vacancies for atomic-level insights into carbon dioxide electroreduction, Nat. Commun. 8 (2017) 1–9.

[37] X. Zhou, Y. Zhong, M. Yang, Q. Zhang, J. Wei, Z. Zhou, Co₂(OH)₂CO₃ nanosheets and CoO nanonets with tailored pore sizes as anodes for lithium ion batteries, ACS Appl. Mater. Inter. 7 (2015) 12022–12029.

[38] T. Tang, W.J. Jiang, S. Niu, N. Liu, H. Luo, Y.Y. Chen, S.F. Jin, F. Gao, L.J. Wan, J. S. Hu, Electronic and morphological dual modulation of cobalt carbonate hydroxides by Mn doping toward highly efficient and stable bifunctional electrocatalysts for overall water splitting, J. Am. Chem. Soc. 139 (2017) 8320–8328.

[39] Z. Yi, J. Ye, N. Kikugawa, T. Kako, S. Ouyang, H. Stuart-Williams, H. Yang, J. Cao, W. Luo, Z. Li, Y. Liu, R.L. Withers, An orthophosphate semiconductor with photooxidation properties under visible-light irradiation, Nat. Mater. 9 (2010) 559–564.

[40] S. Gao, X. Jiao, Z. Sun, W. Zhang, Y. Sun, C. Wang, Q. Hu, X. Zu, F. Yang, S. Yang, L. Liang, J. Wu, Y. Xie, Ultrathin Co₃O₄ layers realizing optimized CO₂ electroreduction to formate, Angew. Chem. Int. Ed. 55 (2016) 698–702.

[41] L.W. Zhang, L. Wang, Y. Zhu, Synthesis and performance of BaAl₂O₄ with a wide spectral range of optical absorption. Adv. Funct. Mater. 17 (2007) 3781–3790.

[42] N. Volz, J. Clayden, The urea renaissance, Angew. Chem. Int. Ed. 50 (2011) 12148–12155.

[43] A.R. Katritzky, A. Oliferenko, A. Lomaka, M. Karelson, Six-membered cyclic ureas as HIV-1 protease inhibitors: a QSAR study based on CODESSA PRO approach, Bioorg. Med. Chem. Let. 12 (2002) 3453–3457.

[44] T. Nagai, N. Mimata, Y. Terada, C. Sebe, H. Shigehisa, Catalytic dealkylative synthesis of cyclic carbamates and ureas via hydrogen atom transfer and radical-polar crossover, Org. Lett. 22 (2020) 5522–5527.

[45] T. Yan, N. Li, L. Wang, Y. Xu, Y. Liang, Y. Dai, B. Huang, J. You, G.A. Ozin, How to make an efficient gas-phase heterogeneous CO₂ hydrogenation photocatalyst, Energ, Environ. Sci. 13 (2020) 3054–3063.

[46] Z. Luo, H. Zhang, Y. Yang, X. Wang, Y. Li, Z. Jin, Z. Jiang, C. Liu, W. Xing, J. Ge, Reactant friendly hydrogen evolution interface based on di-anionic MoS₂ surface, Nat. Commun. 11 (2020) 1–9.

[47] T. Yan, L. Wang, Y. Liang, M. Makaremi, T.E. Wood, Y. Dai, B. Huang, A.A. Jelle, Y. Dong, G.A. Ozin, Polymorph selection towards photocatalytic gaseous CO₂ hydrogenation, Nat. Commun. 10 (2019) 1–10.

[48] S. Salama, T.G. Spiro, Resonance Raman spectra of cobalt (II)-imidazole complexes: analogs of the binding site of cobalt-substituted zinc proteins, J. Am. Chem. Soc. 100 (1978) 1105–1111.

[49] L. Osmieri, A.H.M. Videla, S. Specchia, Activity of Co–N multi walled carbon nanotubes electrocatalysts for oxygen reduction reaction in acid conditions, J. Power Sources 278 (2015) 296–307.

[50] J. Bae, D. Shin, H. Jeong, B.S. Kim, J.W. Han, H. Lee, Highly water-resistant La-doped Co₃O₄ catalyst for CO oxidation, ACS Catal. 9 (2019) 10093–10100.

[51] Y. Fang, X. Chi, L. Li, J. Yang, S. Liu, X. Lu, W. Xiao, L. Wang, Z. Luo, W. Yang, S. Hu, J. Xiong, S. Hoang, H. Deng, F. Liu, L. Zhang, P. Gao, J. Ding, Y. Guo, Elucidating the nature of the Cu (I) active site in CuO/TiO₂ for excellent low-temperature CO oxidation, ACS Appl. Mater. Inter. 12 (2020) 7091–7101.

[52] R. Merryfield, M. McDaniel, G. Parks, An XPS study of the Phillips Cr/silica polymerization catalyst, J. Catal. 77 (1982) 348–359.

[53] C. Pan, J. Xu, Y. Wang, D. Li, Y. Zhu, Dramatic activity of C₃N₄/BiPO₄ photocatalyst with core/shell structure formed by self-assembly, Adv. Funct. Mater. 22 (2012) 1518–1524.

[54] L. Wang, G. Tang, S. Liu, H. Dong, Q. Liu, J. Sun, H. Tang, Interfacial active-site-rich 0D Co₃O₄/1D TiO₂ p-n heterojunction for enhanced photocatalytic hydrogen evolution, Chem. Eng. J. 428 (2022) 131338.

[55] X. Hong, X. Yue, L. Wang, Q. Liu, J. Sun, H. Tang, Lattice-matched CoP/CoS₂ heterostructure cocatalyst to boost photocatalytic H₂ generation, Inorg. Chem. 60 (2021) 12506–12516.

[56] S. Shen, X.L. Wang, Q. Ding, S.Q. Jin, Z.C. Feng, C. Li, Effect of Pt cocatalyst in Pt/TiO₂ studied by in situ FTIR of CO adsorption, Chin. J. Catal. 35 (2014) 1900–1906.

[57] Y. Wang, R. Shi, J. Lin, Y. Zhu, Enhancement of photocurrent and photocatalytic activity of ZnO hybridized with graphite-like C₃N₄, Energ. Environ. Sci. 4 (2011) 2922–2929.

[58] J.B. Peng, F.P. Wu, X.F. Wu, First-row transition-metal-catalyzed carbonylative transformations of carbon electrophiles, Chem. Rev. 119 (2018) 2090–2127.

[59] T. Morimoto, K. Kakiuchi, Evolution of carbonylation catalysis: no need for carbon monoxide, Angew. Chem. Int. Ed. 43 (2004) 5580–5588.

[60] A.E. Sherry, B.B. Wayland, Metalloradical activation of carbon monoxide. formation and carbonyl coupling of a bent 17 electron M-CO unit, J. Am. Chem. Soc. 111 (1989) 5010–5012.

[61] X.Y. Li, X.W. Li, N. Jiao, Rh-catalyzed construction of quinolin-2 (1H)-ones via C-H bond activation of simple anilines with CO and alkynes, J. Am. Chem. Soc. 137 (2015) 9246–9249.

[62] Z. Yin, J.-X. Xu, X.-F. Wu, No making without breaking: nitrogen-centered carbonylation reactions, ACS Catal. 10 (2020) 6510–6531.